Probing the Interatomic Potential of Solids by Strong-Field Nonlinear Phononics

A. von Hoegen[1], R. Mankowsky[1], M. Fechner[1], M. Först[1], A. Cavalleri[1,2]

[1]*Max Planck Institute for the Structure and Dynamics of Matter, 22761 Hamburg, Germany.*
[2]*Department of Physics, University of Oxford, Clarendon Laboratory, Oxford OX1 3PU, UK.*

Nonlinear techniques at optical frequencies have long been applied to condensed matter spectroscopy[1]. As many important excitations of solids are found at low energies, much can be gained from the extension of nonlinear optics to mid-infrared and terahertz (THz) frequencies[2,3]. For example, the nonlinear excitation of lattice vibrations has opened up new perspective to control of materials function dynamically[4-8]. However, only second order phonon nonlinearities[9] at field strengths near 1 MVcm^{-1} have been explored to date. Here, we achieve a one-order-of-magnitude increase in field strength, and excite up to five phonon harmonics of the A_1 phonon mode in $LiNbO_3$. By measuring large amplitude atomic trajectories for this driven mode, we sample the interatomic potential of $LiNbO_3$. These measurements benchmark ab-initio calculations for this material. Tomography of the energy surface by high-order nonlinear phononics will impact many aspects of materials research, including the study of classical and quantum phase transitions.

In the experiments reported in this paper, the highest frequency A_1 mode of $LiNbO_3$ was excited with mid-infrared femtosecond pulses, tuned to 17.5 THz, immediately to the red of the TO phonon frequency (ν_{TO} = 19 THz)[10,11]. In the linear response regime, the real space distortions of this mode involve rotations of the oxygen octahedra, accompanied by *c*-axis motions against the Nb and Li sublattices (see Fig. 1a). Due to the broken inversion symmetry of the crystal, the A_1 mode is both Raman and infrared active[10,11], with electric dipole moment along the *c* axis. In this paper, we explored the response of this mode up to very high amplitudes.

To study the dynamics of the driven mode, we measured time-dependent polarization rotation (PR) and second harmonic (SH) intensity using 30-fs-long probe pulses at 800-nm wavelength. The polarization rotation yielded changes of the dielectric permittivity of the crystal $\varepsilon_r(\tau)$, whereas the second harmonic sampled the changes in the optical second-order susceptibility $\chi^{(2)}(\tau)$ [12,13], and with it the polar component of the lattice motion. Crucially, the stable absolute carrier-envelope-phase[14] of the pump field (Fig. 1b) made it possible to directly follow the atomic trajectories. Spectral interferometry between the PR and SH signal and a local oscillator derived from the same probe pulse yielded both phase and amplitude of these dynamics. The time resolution of these experiments was dictated by the bandwidths of the local oscillators on the detector[15,16], 60 and 80 THz for the SH and PR, respectively. Hence, the measurements were sensitive to the phase of the signal oscillations up to the fifth overtone of the excited TO phonon mode (see Methods section and Extended Data Figs. 1-3 for details).

For small amplitude excitation (0.1 MV/cm), both PR and SH measurements yielded harmonic oscillations (see Fig. 1c and d dashed lines), which were readily attributed to a combination of a 15-THz phonon-polariton and the 19-THz TO phonon of the A_1 mode[17]. As shown in the Methods section (Extended Data Fig. 4), the pump-probe spectrum of the small-field response is

well understood by considering the phase-matching between the probe light and the phonon-polariton propagating into the crystal[18, 19].

At high pump fields (20 MV/cm, Fig. 1c and d solid lines), a strongly anharmonic response was observed, with asymmetric oscillations in both PR and SH signals. Figure 2a and 2b display the corresponding amplitude spectra. In addition to the fundamental frequency components, a number of harmonics appeared. The most pronounced peaks were found at multiples of the 15-THz phonon-polariton mode, visible up to n = 5 (75 THz). Correspondingly, the amplitudes of the first three harmonics at ν = 15, 30 and 45 THz displayed a linear, quadratic and cubic dependence on the excitation field (see Fig.2c). The PR spectrum also exhibited peaks at the sum and difference frequencies of these harmonics (see Extended Data Fig. 5 for a detailed assignments of all peaks). These data are reminiscent of what has been extensively reported in the literature in the context of non-resonant THz and mid-IR harmonic generation[20-25]. However, here the harmonics appear at multiples of the phonon-polariton frequency, instead of the central frequency of the optical pump field, indicating a different physical origin.

To analyze these data, we first consider the local lattice response. We start from the anharmonic lattice potential of the driven mode at ω_{TO}, and ignore phonon-polariton propagation. Ab initio density functional theory (DFT) calculations (see Methods section) yield the anharmonic lattice potential plotted in Fig. 3a. This potential could be fitted by

$$U(Q_{IR}) = \frac{1}{2}\omega_{TO}^2 Q_{IR}^2 + \frac{1}{3}a_3 Q_{IR}^3 + \frac{1}{4}a_4 Q_{IR}^4 + \frac{1}{5}a_5 Q_{IR}^5 \qquad (1)$$

where Q_{IR} denotes the amplitude of the infrared active mode, $\omega_{TO} = 2\pi \cdot \nu_{TO}$, and a_3, a_4 and a_5 are the coefficients of the cubic, quartic and quintic potential term. Note that in the potential of Eq. (1) we have omitted all terms that describe the coupling to other vibrational modes Q_j [5,8,9], of

the form $\sum_j Q_{IR}^2 Q_j$. These terms displace the average lattice structure along all the coupled coordinates Q_j and renormalize the eigenfrequency of the driven mode Q_{IR}. However, as shown in the Extended Data Fig. 6, the effect is small and will not be discussed here.

Starting from the potential energy of Equation (1), we derive the equation of motion for Q_{IR}, considering excitation with a light pulse of carrier frequency ω_{MIR} and duration T

$$\ddot{Q}_{IR} + \gamma \dot{Q}_{IR} + \omega_{TO}^2 Q_{IR} + a_3 Q_{IR}^2 + a_4 Q_{IR}^3 + a_5 Q_{IR}^4 = Z^* E(t) \qquad (2)$$

Here, Z^* denotes the effective charge of the phonon mode, γ is a dissipation constant, and $E(t) = E_0 \sin(\omega_{MIR} t) \cdot \exp(-t^2 / T^2)$ the excitation pulse profile. The calculated dynamics at the 20 MV/cm field strengths used in the experiment are reported in Fig. 3, and predict peaks at harmonics of the fundamental frequency ν_{TO}.

A more comprehensive description of our experimental observations was obtained when propagation effects were taken into account. Finite difference time-domain[26] simulations of phonon-polariton propagation are reported in Figure 4. In these simulations, we combined the linear optical properties of $LiNbO_3$ (Extended Data Table 1) with the nonlinear lattice potential of Eq. (1) (see Methods section and Extended Data Fig. 7). Figure 4a displays the amplitude of the propagating electric field as a function of sample depth d and time t. Both the phonon-polaritons and the broadband radiation emitted from the anharmonic motions propagate from the surface into the bulk, following the dispersion imposed by the material. By integrating the simulated electric field along the 800-nm light line $d_{800} = v_g t$ (red dashed line in Fig. 4a) for each pump-probe time delay τ, we extracted the response shown in Fig. 4b, yielding good qualitative agreement with the polarization-rotation measurement (compare Figs. 4a and 1c). Figure 4c displays the corresponding amplitude spectrum, which comprises peaks at all sum and difference

frequencies of the polariton and the TO mode, also in good agreement with the experiment (see Fig. 2a).

We next turn to the key results of this paper, which are extracted from the time-dependent changes in the second harmonic intensity $I_{SH}(\tau)$. As discussed in References 12, 13 and 27, a coherent phonon of frequency Ω generates frequency-shifted radiation in the second harmonic field E_{SH} due to hyper-Raman scattering. Crucially, the detected spectral interferometry signal is proportional to the lattice *velocity* $I_{SH}(\tau) = B \cdot \dot{\zeta}$ (see also Methods section and Refs. 27, 28). Therefore, one can compare the simulations of Fig. 4 with experiments of Figs. 1d and 2b by spatially integrating the time derivative of the simulated lattice coordinate *Q(t,z)* along the 400-nm light line (Fig. 4d, dashed blue line). This integral was taken over the first 2 μm beneath the surface, where the SH light is generated in the experiment[8]. The corresponding simulated signal $I_{SH}(\tau)$ (Fig. 4e) contains frequency components at multiples of 16 and 19 THz (see Fig. 4f), in agreement with the measured data of Fig 2b.

Most importantly, from the knowledge of $\dot{\zeta}$, the microscopic lattice potential *U(Q)* explored during each oscillation cycle could be reconstructed. We consider the coherent dynamics of the lattice at times *after* the pump pulse, that is when no force is being applied onto the mode. For weak phonon damping (γ), the total energy of the unforced oscillating lattice can be approximated as being constant over each cycle $U(\tau) + E_{kin}(\tau) = \varepsilon$. Hence, we could retrieve the instantaneous potential energy $U(\tau) = \varepsilon - E_{kin}(\tau)$ from the knowledge of the kinetic energy, which is in turn proportional to the square of the measured second harmonic signal $E_{kin}(\tau) = \frac{1}{2}\dot{\zeta}$ $\frac{1}{2} I_{SH}(\tau)^2 / B^2$. The instantaneous potential energy $U(\tau)$, which was known except for a proportionality term $1/B^2$, could then be converted into $U(Q)$ by a time integral of the

second harmonic signal $I_{SH}(\tau) = B \cdot \dot{Q}^2$, which yielded $Q(\tau)$. Hence, we could extract the shape of the lattice potential bar a single proportionality constant. Since different cycles with different amplitudes and different total energy ε trace fractions of the potential energy $U(Q)$ many times, the shape of the potential reconstructed in this way was highly over-determined.

Figure 5 compares the lattice potential of the A_1-mode calculated from DFT (grey line) to the reconstructed potential (filled circles). The calculated and reconstructed curves were matched by adjusting one free parameter B (see Methods for details). Within the systematic uncertainties of DFT calculations (grey shaded area), we find agreement between the shapes of the anharmonic potentials up to the highest amplitudes reached experimentally.

The tomography of the force field discussed above is straightforwardly extensible to all materials with a large bandgap, like ferroelectrics, for which acceleration of quasi-particles in the field is neglected to first order. We note that direct measurements of the coordinate $Q(\tau)$ with femtosecond x-ray diffraction, for example from a free electron laser with pulses that are appropriately synchronized with the absolute phase of a strong THz field, would allow for an unbiased measurement of the potential, without the need of comparing the data to a calculated potential and determination of the constant. Also, full reconstruction of the force field of a material with N atoms requires the measurement of 3N-3 lattice modes without symmetry considerations. Recent advances in the generation of mid-infrared and THz pulses that are both widely tunable and intense[29], make these prospects realistic. Tomographic measurements of force potentials in the vicinity of equilibrium phase transitions will yield crucial information not accessible otherwise. Finally, as the sampling of the potential can be retrieved within one cycle of the pump light, one could envisage measurements of rapidly evolving potential energy surfaces.

References

1. Shen, Y. R. The Principles of Nonlinear Optics (Wiley-Interscience ,Hoboken, 2002)

2. Kampfrath, T. ,Tanaka, K. & Nelson, K. A. Resonant and nonresonant control over matter and light by intense terahertz transients. Nat. Photon. 7, 680-690 (2013).

3. Nicoletti, D., Cavalleri, A. Nonlinear light–matter interaction at terahertz frequencies. Adv. Opt. Photonics 8, 401-464 (2016).

4. Mitrano, M. et al. Possible light-induced superconductivity in K_3C_{60} at high temperature. Nature 530, 461-464 (2016).

5. Mankowsky, R. et al. Nonlinear lattice dynamics as a basis for enhanced superconductivity in $YBa_2Cu_3O_{6.5}$. Nature 516, 71-73 (2014).

6. Nova, T. F. et al. An effective magnetic field from optically driven phonons. Nature Physics, 13, 132–136 (2017).

7. Fausti, D. et al. Light induced Superconductivity in a Stripe-ordered Cuprate. Science 331, 189-191 (2011).

8. Mankowsky, R., von Hoegen, A., Först, M. & Cavalleri, A. Ultrafast reversal of the ferroelectric polarization. Phys. Rev. Lett. , (2017).

9. Först, M. et al. Nonlinear phononics as a new ultrafast route to lattice control. Nat. Phys. 7, 854-856 (2011).

10. Schaufele, R. F. & Weber, M. J. Raman scattering by lithium niobate. Phys. Rev. 152, 705-708 (1966)

11. Barker, A. S. and Loudon, R. Dielectric properties and optical phonons in LiNbO3. Phys. Rev.158, 433-445, 1967.

12. Chang, Y.-M., Xu, L. & Tom, H. W. K. Observation of local-interfacial optical phonons at buried interfaces using time-resolved second-harmonic generation. Phys. Rev. B 59, 12220-12223 (1999).

13. Denisov, V. N. , Mavrin, B. N. & Podobedov, V. B. Hyper-Raman by vibrational exciations in crystals, glasses and liquids. Phys. Rep. 151, 1-92 (1987).

14. Sell, A., Leitenstorfer, A. & Huber, R. Phase-locked generation and field-resolved detection of widely tunable terahertz pulses with amplitudes exceeding 100 MV/cm. Opt. Lett. 33, 2767–2769 (2008).

15. Keiber, S. et al. Electro-optic sampling of near-infrared waveforms. Nat. Photon. 10, 159-163 (2016)

16. Porer, M., Ménard, J.-M. & Huber, R. Shot noise reduced terahertz detection via spectrally postfiltered electro-optic sampling. Opt. Lett. 39, 2435-2438 (2014)

17. Kojima, S., Kanehara, K., Hoshina, T. & Tsurumi, T. Optical phonons and polariton dispersions of congruent LiNbO3 studied by far-infrared spectroscopic ellipsometry and Raman scattering. Jpn. J. Appl. Phys. 55, 1-5 (2016).

18. Claus, R. Light scattering by optical phonons and polaritons in perfect crystals. phys. stat. sol. (b) 50, 11-32 (1972).

19. Dastrup, B. S., Hall, J. R. and Johnson, J. A., Experimental determination of the interatomic potential in $LiNbO_3$ via ultrafast lattice control. Appl. Phys. Lett. 110, 162901 (2017).

20. Ghimire, S. et al. Observation of high-order harmonic generation in a bulk crystal. Nat. Phys. 7, 138–141 (2011).

21. Schubert, O. et al. Sub-cycle control of terahertz high-harmonic generation by dynamical Bloch oscillations. Nat. Photon. 8, 119–123 (2014)

22. Zaks, B., Liu, R. B. & Sherwin, M. S. Experimental observation of electron–hole recollisions. Nature 483, 580–583 (2012)

23. Vampa, G. et al. Linking high harmonics from gases and solids, Nature 522, 462–464, (2015).

24. Itatani, J. et al. Tomographic imaging of molecular orbitals, Nature 432, 867–871, (2004).

25. Langer, F. et al. Lightwave-driven quasiparticle collisions on a subcycle timescale, Nature 533, 225-229, (2016)

26. Taflov, A., Hagness, S. C. Computational electrodynamics: the finite-difference time-domain method (Artech House, Boston, 2000)

27. Yan, Y.X., Gamble Jr., E. B. & Nelson, K. A. Impulsive stimulated scattering: General importance in femtosecond laser pulse interactions with matter, and spectroscopic applications. J. Chem. Phys. 83, 5391-5399 (1985).

28. Merlin, R. Generating coherent THz phonons with light pulses. *Solid State Commun.* **102**, 207–220 (1997).

29. B. Liu et al. Generation of narrowband, high-intensity, carrier-envelope phase stable pulses tunable between 4 and 18 THz. Optics Letters 42, 129-131 (2017)

Acknowledgements

We thank Roberto Merlin and Massimo Altarelli for valuable discussions. The research leading to these results received funding from the European Research Council under the European Union's Seventh Framework Programme (FP7/2007–2013)/ERC Grant Agreement No. 319286 (QMAC). This work has been supported by the excellence cluster "The Hamburg Centre for Ultrafast Imaging—Structure, Dynamics and Control of Matter at the Atomic Scale" of the Deutsche Forschungsgemeinschaft.

Author Contributions

A.C. conceived this project together with A.v.H. and R.M.. R.M., A.v.H. and M. Först built the experimental setup. A.v.H. and R.M. conducted the experiment and analysed the data. M. Fechner performed the DFT calculations. A.v.H. conducted the FDTD simulation. All authors contributed to the manuscript.

Author Information

Reprints and permissions information is available at www.nature.com/reprints. The authors declare no competing financial interests. Readers are welcome to comment on the online version of the paper. Correspondence and requests for materials should be addressed to A.C. (andrea.cavalleri@mpsd.mpg.de) or A.v.H. (alexander.von-hoegen@mpsd.mpg.de).

Figure Captions

Figure 1| Experimental setup and time-resolved optical changes. a, Schematic of the pump-probe geometry. The resonantly excited A_1 phonon mode in $LiNbO_3$ is also shown with a polar component along the crystal c axis. **b**, Electro-optic sampling measurement of the 150 fs, carrier envelope phase stable mid-infrared pump pulses, centered at 17.5 THz with 4 THz bandwidth. **c** and **d**, Time-resolved polarization rotation of the 800-nm probe and changes of the second harmonic intensity, both for high (solid colored lines) and low (dashed lines) excitation fields.

Figure 2| Amplitude spectra and excitation field dependence. a and **b**, FFT amplitude spectra of the polarization rotation and second harmonic intensity measurements, both for the high excitation field shown in Figure 1. The blue and read peaks correspond to multiples of the phonon-polariton frequencies ν_p (15.3 THz at 800 nm, 16.2 THz at 400 nm) and ν_{TO}, respectively. The grey peaks in panel **a** label sum and difference frequencies of ν_p and ν_{TO}, which are absent in the SH response. **c**, Excitation field dependence of the peak area at the first, second and third harmonic of ν_p, revealing a linear, quadratic and cubic dependence. Error bars represent the standard deviation σ calculated from the noise level of the experiment.

Figure 3| Anharmonic lattice potential. Calculated lattice potential energy of $LiNbO_3$ (red) of the A_1 mode shown in Fig. 1a, compared to a harmonic potential (grey) with the same fundamental frequency ω_{TO}. The arrows denote the expected positive and negative excursions for an energy of 0.6 eV, corresponding to the energy deposited per unit cell by the excitation pulses. The lower graph shows the solution of the equation of motion and its amplitude spectrum.

Figure 4| FDTD phonon-polariton propagation simulations. a, Contour plot of the electric field as a function of depth d and time t inside $LiNbO_3$ after mid-infrared excitation. The red dashed line shows the propagation of the 800-nm probe pulse for one pump-probe time delay τ, following the relation $d_{800} = v_g t$ with v_g the group velocity. **b**,**c** Time trace derived by integrating along the dashed red line in panel a for all pump-probe delays and the corresponding amplitude spectrum. The spectrum shows harmonics of ν_p and ν_{TO} as well as mixed frequencies. **d**, Contour plot of the vibrational amplitude Q_{IR} after the same mid-infrared excitation as in panel **a**. The dashed blue line shows the propagation of the SH light at 400 nm, also for a single time delay τ. **e**, Time trace derived by spatially integrating the time derivative of Q_{IR} along the dashed blue line within the first 2 μm for all pump probe delays. **f**, Amplitude spectrum of panel e, which only shows broad peaks at the harmonics of ν_p and ν_{TO}.

Figure 5| Reconstructed A_1 mode potential energy. Potential energy of the A_1 mode (red colored circles) reconstructed from different cycles of the time-resolved SH measurement shown in the inset. Error bars represent the standard deviation σ calculated from the noise level of the experiment. The grey solid line is the mode potential obtained by DFT calculations and the grey shaded area is an estimate of its systematic uncertainties. The experimental potential is scaled to the calculated potential using a single scaling factor (see Methods section). From this comparison, we estimate maximum mode excursions of 1.4 $Å\sqrt{amu}$, corresponding to ~14 pm displacements of the oxygen atoms from their equilibrium positions. The dashed curve is the potential in the harmonic approximation.

Methods

Experimental Setup

The carrier envelope phase (CEP) stable 150-fs long 17.5-THz mid-infrared pump pulses of 4 THz bandwidth were obtained by mixing the two signal beams from two optical parametric amplifiers, which were seeded by the same white light and pumped by 30-fs, 800-nm pulses at 1 kHz repetition rate. The nonlinear lattice dynamics in $LiNbO_3$ were probed by a time-delayed replica of the 800-nm pulses, in non-collinear geometry with an angle of 30° to the mid-IR pump (see Extended Data Fig. 1). The CEP stability of the excitation pulse is reflected in phase stability of the resonantly driven coherent oscillations of the A_1 phonon mode.

The pump induced polarization rotation of the 800-nm beam was measured by detecting the time-resolved difference signal of two intensity-balanced photodiodes placed behind a half-wave plate and a Wollaston prism.

Due to the large second-order nonlinear susceptibility of $LiNbO_3$, the 800-nm probe pulses also generated second harmonic (SH) light at 400 nm, which was separated from the fundamental beam after the sample by a dichroic mirror and detected with a photo multiplier tube. The SH signal originates from a layer of one coherence length l_c = 1.3 μm below the surface[8,30].

All experiments were conducted at room temperature. The sample used in the experiments was a commercially available congruent $LiNbO_3$ single crystal (5x5x5 mm^3).

Polarization rotation and second harmonic detection processes

The nonlinear interaction of a lattice vibrational mode with an optical probe pulse involves Raman scattering in polarization rotation measurements and hyper-Raman scattering in second harmonic measurements[12,13,27,28]. These processes can be described by the wave equation

$$\frac{\partial^2 E}{\partial z^2} - \frac{n^2}{c^2}\frac{\partial^2 E}{\partial t^2} = \rho \frac{\partial^2 (E_{\text{probe}} Q)}{\partial t^2},$$

where n is the refractive index of the material and c the vacuum speed of light. The constant ρ contains the number density of oscillators and the Raman cross-section. E_{probe} denotes the probe laser field at angular frequency ω_{probe} (Refs. 27,28), i.e. the fundamental 800-nm light in the PR measurement and the second harmonic 400-nm light in the SH measurement. $Q(z,t+\tau) = Q_0(z) \cdot \sin(\Omega \cdot (t+\tau))$ is the time-dependent amplitude of the excited vibrational mode, with τ the time delay between pump and probe pulses. A general solution to this equation is

$$E(z,t) = E_{\text{probe}}(z,t) - c\frac{\partial}{\partial t}(Q(z,t+\tau)\cdot E_{\text{probe}}(z,t))^{27,28},$$

showing that the probe electric field is modulated by the time derivative of $Q(z,\ t+\tau)\cdot E_{\text{probe}}(z,t)$. After interaction with a phonon-polariton of frequency Ω and at a specific time delay, the spectrum of the transmitted probe, which is the Fourier transform of $E(z,t)$, reads

$$E(\omega) = E_{\text{probe}}(\omega) + \beta\cdot\omega\cdot(E_{\text{probe}}(\omega+\Omega)\cdot\exp(i\Omega\cdot\tau) - E_{\text{probe}}(\omega-\Omega)\cdot\exp(-i\Omega\cdot\tau)).$$

It contains the unperturbed probe spectrum $E_{\text{probe}}(\omega)$ and sidebands generated at $\omega_{\text{probe}} \pm \Omega$. Importantly, these sidebands acquire a time delay dependent phase $\exp(\pm i\Omega\tau)$. Their phase sensitive detection, for example achieved by spectral interference with the local oscillator

$E_{\mathrm{probe}}(\omega)$ on the detector, carries information about both phase and amplitude of the phonon-polariton[15,16].

In this case, the measured intensity at a time delay τ is

$$I(\tau) = \int d\omega \left(\left| E_{\mathrm{probe}}(\omega) + \beta \cdot \omega \cdot (E_{\mathrm{probe}}(\omega+\Omega) \cdot \exp(i\Omega \cdot \tau) - E_{\mathrm{probe}}(\omega-\Omega) \cdot \exp(-i\Omega \cdot \tau)) \right|^2 \right).$$
$$= I_{\mathrm{probe}} + \alpha \cdot \Omega \cdot \cos(\Omega \cdot \tau) + \gamma \cdot \Omega^2 \cdot \cos(2\Omega \cdot \tau)$$

We disregard the homodyne component proportional to $\gamma \cdot \Omega^2$, which is far smaller than the heterodyne component, proportional to $\alpha \cdot \Omega$[32]. Hence, the detected interference signal is

$$I(\tau) = I_{\mathrm{probe}} + \alpha \cdot \Omega \cdot \cos(\Omega \cdot \tau)$$ [27,28,31].

Crucially, this time delay dependent signal is $\pi/2$ phase shifted and amplitude scaled $\propto \Omega$ with respect to the lattice vibration $Q(t) = Q_0 \cdot \sin(\Omega \cdot (t+\tau))$. Hence, it is proportional to the velocity of the vibrational motion $\dot{Q}(\tau)$. For in-depth discussion we refer to Refs. 27, 28, and 31.

In the PR measurements, the detected difference signal is $\Delta I(\tau) = I_{\parallel}(\tau) - I_{\perp}(\tau) = 2\alpha \cdot \Omega \cdot \cos(\Omega \cdot \tau)$. The time resolution is determined by the bandwidth of the local oscillator at the detector[15,16] that is spectrally broadened with respect to the incident pulse due to self-phase modulation in the LiNbO3 crystal[32,33] (see Extended Data Fig. 3a). The sampling efficiency, calculated according to Ref. 15 and shown in Extended Data Fig. 3b, allows efficient detection up to 80 THz. Further, the interaction length between the 800-nm probe and the phonon-polariton harmonics is determined by the penetration depths, which increase with increasing harmonic order (see also Extended Data Fig. 3b). As result, the PR measurements cannot be used to quantify the amplitude of the atomic motions in a straightforward manner.

In the SH measurement, the detected light is generated in a thin layer of 1.3 μm below the sample surface[8,30]. Therefore, the interaction length with the phonon-polariton harmonics does not change for different harmonic orders. The SH bandwidth supports efficient detection up to 60 THz (see Extended Data Fig. 3c and d). A bandpass filter was used to shape the spectral response function in order to flatten the sampling efficiency for the first three harmonics[15,31].

The phonon-polariton induced oscillatory signal components were extracted from the $I_{SH}(\tau)$ data via subtraction of a slowly varying background, which results from the modification of $\chi^{(2)}$ due to changes in the ferroelectric polarization (see Ref. 8).

Phase-matching between the probe light and the phonon-polariton

The amplitude spectra shown in Extended Data Figure 4 are well understood by considering the phase-matching between the probe light and the phonon-polariton propagating into the crystal. The phonon-polariton dispersion of $LiNbO_3$ (black line) is plotted as $\nu_p = \frac{c_0}{\sqrt{\varepsilon(\nu)}} q$, where c_0 is the vacuum speed of light and $\varepsilon(\nu)$ the dielectric function. The light lines $\nu = v_g\, q$ of the 800 nm (red, $v_{g,800} = c_0/2.3$) and the 400 nm (blue, $v_{g,400} = c_0/3.03$) probe fields are also shown, where v_g and q denote the group velocity and wave number, respectively. Phase-matching occurs at those frequencies for which the light lines intersect the phonon-polariton dispersion curve[18,34], i.e. at 15 THz (PR), 16 THz (SH) and 19 THz (both PR and SH).

Assignment of all peaks in the PR amplitude spectrum

Extended Data Figure 5 displays a detailed assignment of all peaks in the amplitude spectrum of the polarization rotation measurement. Circles/triangles represent a shift of the probe light by ν_p and ν_{TO}, respectively. Multiple symbols indicate a shift by multiples of the fundamental

frequency. Blue and red colors indicate up and down shifts, corresponding to sum and difference frequency mixing, respectively.

Linear Optical Properties

The low-frequency linear optical properties for light polarized along the $LiNbO_3$ c-axis are dominated by two optical phonon modes at 7.8 and 18.9 THz. It also includes a weak mode at 8.2 THz and a feature at 21 THz, which has been attributed to two-phonon absorption[11]. Extended Data Fig. 7 shows the THz reflectivity spectrum of the investigated sample (grey line), measured via Fourier transform infrared spectroscopy (FT-IR), together with fits of four (red line) and two (blue line) Lorentzian oscillators. The fit parameters for the two dominating optical phonons (listed in Extended Data Table 1) were used in the finite difference time domain (FDTD) simulations of the phonon-polariton propagation. The reflectivity spectrum simulated from the parameters of these two oscillators (green line) agrees with the experimental data within the region of interest (12-20 THz).

FDTD phonon polariton simulations

The phonon-polariton propagation dynamics in $LiNbO_3$ have been calculated by solving Maxwell's equations in space and time. To this end we used FDTD in one spatial dimension[26].

We modeled the linear response of the material using the parameters of the two dominant optical phonons obtained from fitting the FT-IR measurement (see above). For each mode, the equation of motion is given by

$$\ddot{\xi}_{IR} + \gamma \dot{\xi}_{IR} + \omega_{TO}^2 \xi_{IR} = Z^* E(t).$$

Here, γ is the damping constant, ω_{TO} the phonon angular frequency and Z^* the born effective charge, which can be expressed as $\omega_{TO}\sqrt{(\varepsilon_0 - \varepsilon_\infty)}\sqrt{\frac{\epsilon_0}{n}}$ with n the oscillator density, ϵ_0 the

vacuum permittivity, and ε_0 and ε_∞ the low and high frequency limits of the dielectric function, respectively. The oscillator density was approximated as one oscillator per unit cell. For each mode, ε_0 and ε_∞ were derived from the generalized Lydanne-Sachs-Teller relation[35].

The above equation was solved at every discrete point of the grid in space and time using the values of the electric field calculated from Maxwell's equation. The oscillator equation and Maxwell's equation are coupled via the electric displacement field

$$D = \in_0 \varepsilon_\infty E + \omega_{TO}\sqrt{(\varepsilon_0 - \varepsilon_\infty)}\sqrt{\in_0 n}\cdot Q_{IR} \ .$$

The linear optical properties of $LiNbO_3$ are well reproduced by our simulation (see Extended Data Fig. 7).

Nonlinear effects were captured by introducing the lattice anharmonicities of the driven A_1 mode into the above equation of motion:

$$\ddot{Q}_{IR} + \gamma \dot{Q}_{IR} + \omega_{TO}^2 Q_{IR} + a_3 Q_{IR}^2 + a_4 Q_{IR}^3 + a_5 Q_{IR}^4 = Z^* E(t) \, .$$

The anharmonic coefficients a_3, a_4 and a_5 are taken from ab-initio Density Functional Theory calculations as described below (a_3 = 1567.65 meV/amu$^{3/2}$/Å^3, a_4 = 900.8 meV/amu^2/Å^4, a_5 = 7.1 meV/amu$^{5/2}$/Å^5). Here, the mid-infrared pump pulse was set to a field strength of 30 MV/cm, carrier frequency 17.5 THz and 180 fs duration, comparable to the experiment.

We evaluated the equations in time steps of 0.5 fs and with a spatial grid of 0.5 μm. Perfectly matched boundary conditions were implemented to impede back reflection.

DFT calculations of the full anharmonic potential

To explore the nonlinear response of a resonantly excited phonon mode we performed first-principle computations within the framework of density functional theory (DFT). All our computations were carried out using DFT as implemented in the Quantum Espresso code[36]. We used ultrasoft pseudopotentials, which contain as valence states the 2p 2s for Lithium, $4s^2 4p^6 4d^4 5s^1$ for Niobium and $2s^2 2p^4$ for Oxygen. As numerical parameters, we applied a cutoff energy for the plane wave expansion of 80 Rydberg and five times this value for the charge density. For all computations, we sampled the Brillouin zone by a 17x17x17 k-point mesh generated with the Monkhorst and Pack scheme[37] and reiterated total energy calculations until the total energy became less than 10^{-10} Rydberg. Before calculating phonon-modes we fully structural relaxed the unit-cell regarding forces and pressure below the threshold of 5 $\mu Ry/a_0$. We finally performed density functional perturbation theory[38] calculations to obtain phonon modes eigenvectors and frequencies. Finally, we compute the anharmonic phonon potential by calculating the total energy for structures, which have been modulated with the phonon eigenvector. Least mean square fits of this total energy landscape reveal the anharmonic coefficients of Eq. (2) of the main text and the phonon mode eigenvector as shown in Fig. 1a.

Scaling the reconstructed potential

The unknown proportionality factor *B,* which connects the measured SH signal to the vibrational velocity via $I_{SH}(\tau) = B \cdot \dot{Q}(\tau)$, leaves a single scaling factor to the reconstruction. The kinetic energy becomes $E_{kin}(\tau) = \frac{1}{2}\frac{(I_{SH}(\tau))^2}{B^2}$ and the vibrational amplitude $Q(\tau) = \int I_{SH}(\tau)/B d\tau$. Hence, the y-axis of the reconstruction will be scaled with B^2 and the x-axis with B to the correct absolute values. This constant B can most effectively be derived by fitting the function $f(Q)$ =

$1/B^2 \cdot U(B \cdot Q)$ to the experimental data, where *U(Q)* is the potential obtained by DFT. Once *B* is retrieved, the experimental x and y axis can be rescaled to the absolute phonon amplitude in terms of Å $\sqrt{amu}$ and the potential energy in eV, respectively.

The maximum displacement of the oxygen atoms involved in the A_1 vibrational mode was calculated with the knowledge of the phonon eigenvectors, which we obtained from DFT calculations. We find a maximum displacement of the oxygen atoms of approximately 14 pm, which amounts to 7% of the Nb-O and 5% of the O-O nearest neighbor distance at the corresponding potential energy (0.7 eV), which agrees with the estimated energy deposited per unit cell (0.6 eV at 3 μJ pulse energy).

Effect of inter-phonon coupling of the type $g_j \cdot Q_{IR}^2 Q_j$

Besides the nonlinearities of the driven lattice mode, the full lattice potential also comprises coupling to other phonon modes of the form $g_j \cdot Q_{IR}^2 Q_j$:

$$U(Q_{IR}, Q_j) = \frac{1}{2}\omega_{TO}^2 Q_{IR}^2 + \frac{1}{3}a_3 Q_{IR}^3 + \frac{1}{4}a_4 Q_{IR}^4 + \frac{1}{5}a_5 Q_{IR}^5 + \sum_j \frac{1}{2}\omega_j^2 Q_j^2 + \sum_j g_j \cdot Q_{IR}^2 Q_j \quad .$$

Here, Q_j denotes the amplitude of a coupled lattice mode and ω_j its resonance frequency[5,8,9]. For strongly driven Q_{IR} the nonlinear interaction leads to a directional force on the coupled mode Q_j, which can be used to control materials' functionality[8].

In addition, the finite amplitude Q_j renormalizes the fundamental frequency of Q_{IR}, as can be seen in the equations of motion

$$\ddot{Q}_{IR} + \gamma_{IR}\dot{Q}_{IR} + (\omega_{TO}^2 - 2g \cdot Q_R)Q_{IR} = Z^* E(t)$$
$$\ddot{Q}_j + \gamma_j \dot{Q}_j + \omega_j^2 Q_j = g_j \cdot Q_{IR}^2$$

This frequency renormalization $\omega'_{TO} = \sqrt{(\omega_{TO}^2 - 2g \cdot Q_R)}$ was observed in our experiment with a maximum change of 3.5% at the highest driving field (see. Extended Data Fig. 6).

Data availability. The data that support the findings of this study are available from the corresponding author upon reasonable request.

Method References

30. Mlejnek, M., Wright, E. M., Moloney, J. V. & Bloembergen, N. Second Harmonic Generation of Femtosecond Pulses at the Boundary of a Nonlinear Dielectric, Phys. Rev. Lett. 83, 2934 (1999).

31. Wahlstrand, J. K , Merlin, R., Li, X., Cundiff, S. T. & Martinez, O. E. Impulsive stimulated Raman Scattering: compariosn between phase-sensitive and spectrally filtered techniques, Opt. Lett. 30, 926 (2005).

32.Träger, F. *Springer handbook of lasers and optics* (Springer, New York, 2007).

33. Dharmadhikari, J. A., Dota, K., Mathur, D. & Dharmadhikari A. K. Spectral broadening in lithium niobate in a self-diffraction geometry using ultrashort pulses. Appl. Phys. B 140, 122-129 (2016).

34. Stevens, T., Wahlstrand, J. K. & Merlin, R. Cherenkov radiation at speeds below the light threshold: Phonon-assisted phase matching. Science 291, 627-630 (2001).

35. Chaves, A. S. & Porto, S. P. S. Generalized Lyddane-Sachs-Teller relation. Solid State Commun. 13, 865-868 (1973).

36. Giannozzi, P. et al. QUANTUM ESPRESSO: a modular and open-source software project for quantum simulations of materials. J. Phys. Condens. Matter 21, 395502 (2009).

37. Monkhorst, H. & Pack, J. Special points for Brillouin-zone integrations. Phys. Rev. B 13, 5188 (1976).

38. Baroni, S., de Gironcoli, S., Dal Corso, A. & Giannozzi, P. Phonons and related crystal properties from density-functional perturbation theory. Rev. Mod. Phys. 73, 515 (2001).

Extended Data Table 1 Values obtained from a fit of four Lorentzian oscillators to the reflectivity spectrum of our $LiNbO_3$ sample.

Extended Data Figure 1 Schematic representation of the experimental setup. 30-fs pulses from a Ti:sapphire amplifier are used to pump two optical parametric amplifiers (OPA), which are seeded by the same white light continuum (WLC) . Carrier envelope phase stable 3-μJ 150-fs pulses at 17 μm wavelength are obtained by difference frequency generation of the two signal beams from the OPAs. The mid-infrared light is focused to a spotsize of approximately 65 μm using a telescope and overlapped with the 800-nm probe beam (40 nJ, 35 μm spotsize).

Extended Data Figure 2 The black solid line is the incident spectrum of the 800-nm probe pulses with a bandwidth of ~ 30 THz. The grey solid lines are the sidebands generated from the phonon harmonics measured at different positions behind the $LiNbO_3$ crystal. Due to momentum conservation, each sideband propagates in slightly different direction compared to the unperturbed 800 nm beam. The red line is a guide to the eye of the resulting spectral broadening.

Extended Data Figure 3 a, Spectrum of the 800-nm probe pulse before (red) and after (grey) propagation through the unpumped $LiNbO_3$ crystal in units of THz. **b**, Red curve: sampling efficiency of the 800-nm light calculated with the spectrum shown in panel a. The grey curve is the penetration depth in the mid-infrared region obtained from FT-IR spectroscopy. **c**, Spectrum of the generated SH light (blue curve) and normalized transmission of the bandpass filter placed in front of the detector (dashed curve), also shown in units of THz. **d**, Sampling efficiency of the SH light with the spectrum shown in panel c. The sampling efficiency is almost constant in the 15-45 THz region of the first three phonon harmonics.

Extended Data Figure 4, Phonon-polariton dispersion of the two dominant lattice modes in $LiNbO_3$ (black curve) and two light lines $\nu = v_g\, q$ for 800 nm (red) and 400 nm (blue)

wavelengths. The dots mark the points of intersection with the dispersion relation, which correspond to the observed fundamental frequencies of the driven mode (left and right panel).

Extended Data Figure 5 Amplitude spectrum of the time-resolved polarization rotation measurement. Blue symbols denote a blueshift of 15 THz (triangles) and 19 THz (circles). Multiple symbols represent shifts by multiples of the corresponding frequencies. Red symbols denote red shifts.

Extended Data Figure 6 The black circles denote the peak-field dependent fundamental phonon frequencies extracted from Fourier transformations of the time-resolved signals. Values at the same frequency have been binned (red circles) to account for the limited frequency resolution of the FFT analysis. The error bars denote 1σ (67% confidence interval). The grey line is fit to the data with the function $f(E) = \sqrt{1 + a \cdot E^2}$.

Extended Data Figure 7 The grey solid line is the measured THz reflectivity spectrum of $LiNbO_3$ with light polarized along the c axis. The red line is a fit considering four Lorentzian oscillators. The dashed blue line is a fit considering only the two dominant phonon modes at 7.5 and 19 THz. The green line is the FDTD simulated reflectivity when only these two oscillators are considered (see Methods section).

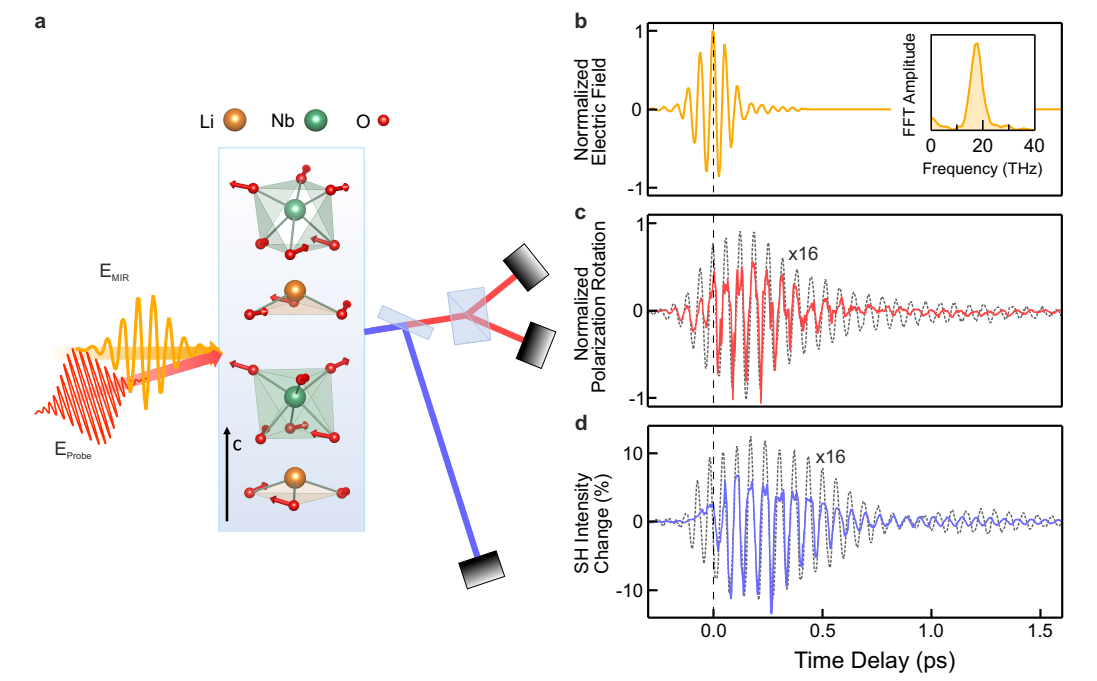
a
Li
Nb
O
E_MIR
E_Probe
c
b
Normalized Electric Field
1
0
-1
FFT Amplitude
0
20
40
Frequency (THz)
c
Normalized Polarization Rotation
x16
1
0
-1
d
SH Intensity Change (%)
x16
10
0
-10
0.0
0.5
1.0
1.5
Time Delay (ps)

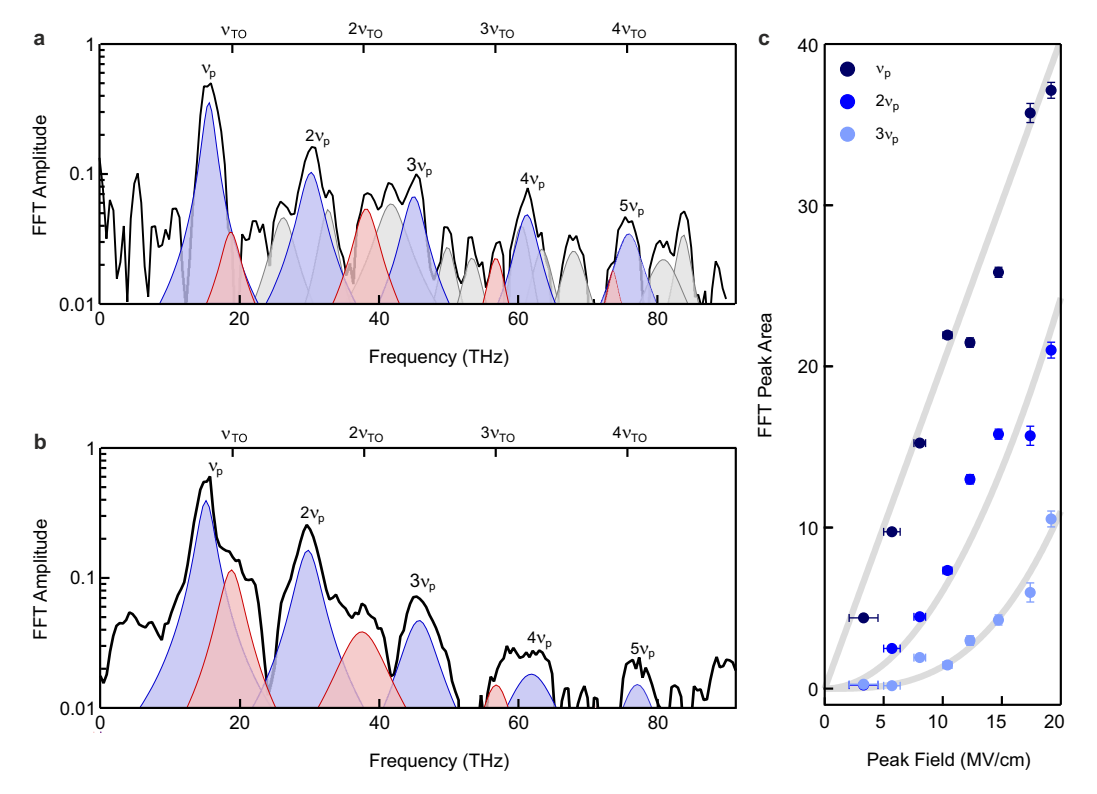
a
b
c
ν_{TO}
$2\nu_{TO}$
$3\nu_{TO}$
$4\nu_{TO}$
ν_p
$2\nu_p$
$3\nu_p$
$4\nu_p$
$5\nu_p$
FFT Amplitude
Frequency (THz)
FFT Peak Area
Peak Field (MV/cm)

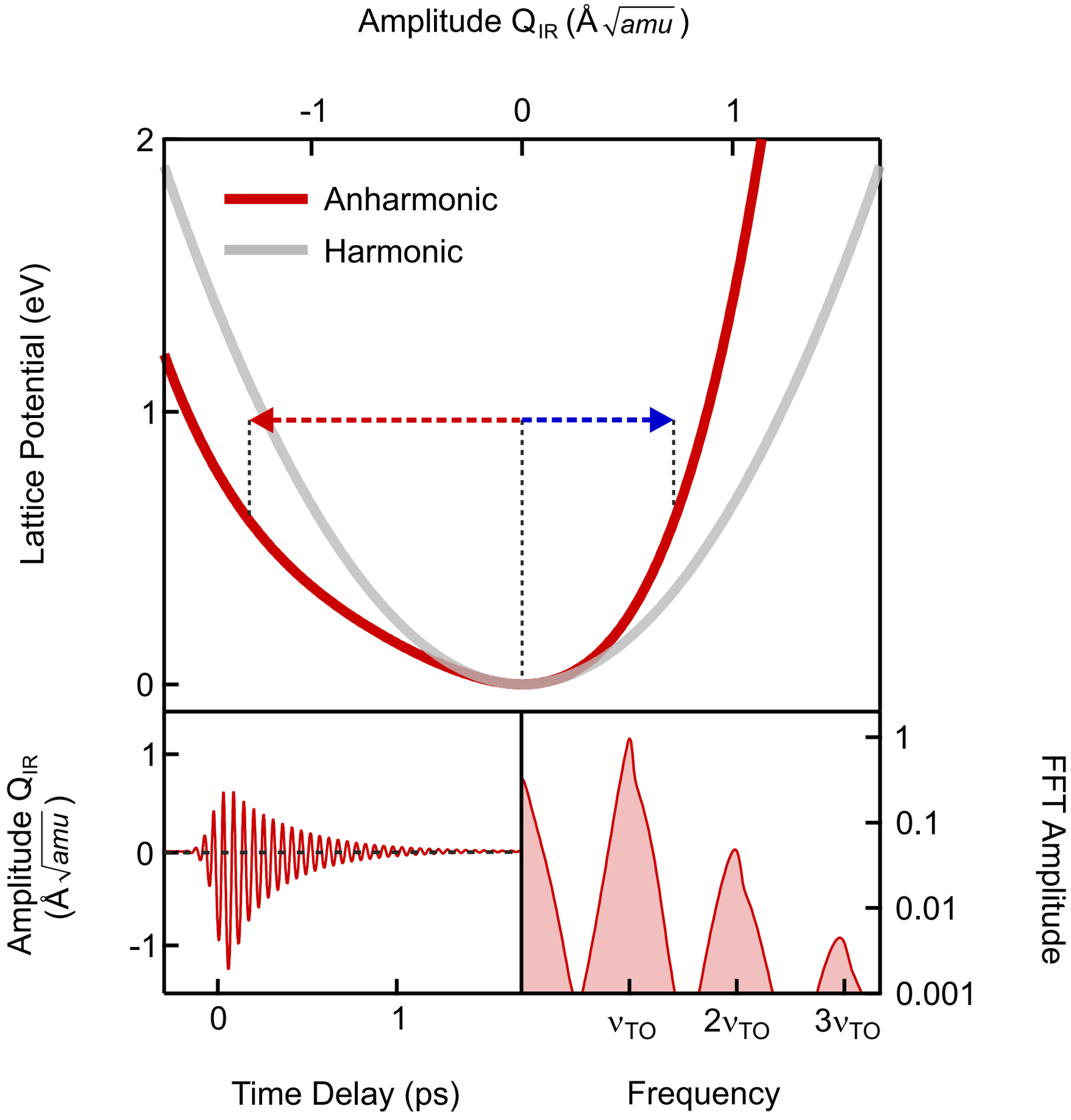
Amplitude Q_{IR} (Å $\sqrt{amu}$)
-1
0
1
2
1
0
Anharmonic
Harmonic
Lattice Potential (eV)
1
0
-1
Amplitude Q_{IR} (Å $\sqrt{amu}$)
0
1
Time Delay (ps)
ν_{TO}
$2\nu_{TO}$
$3\nu_{TO}$
Frequency
1
0.1
0.01
0.001
FFT Amplitude

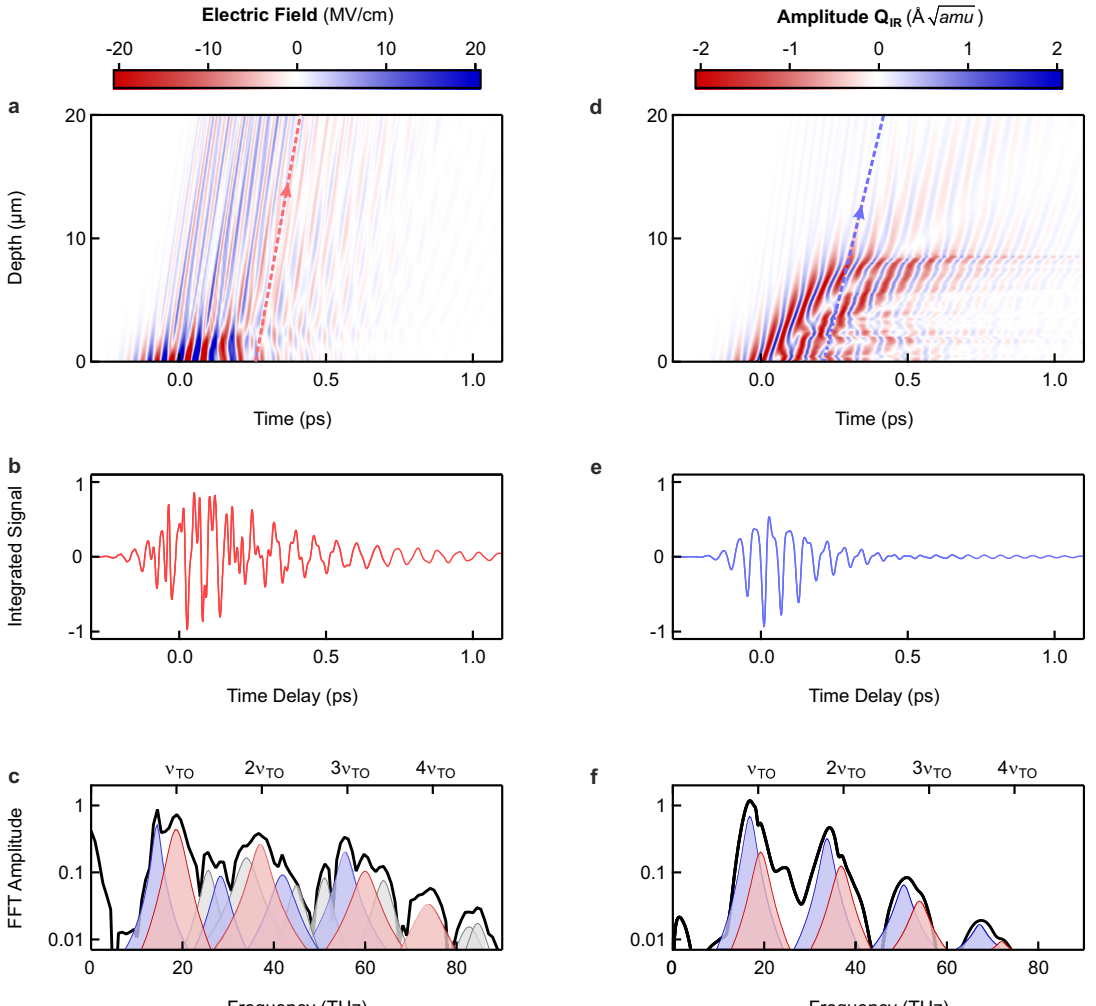
Electric Field (MV/cm)
-20
-10
0
10
20
a
Depth (μm)
20
10
0
0.0
0.5
1.0
Time (ps)
b
Integrated Signal
1
0
-1
0.0
0.5
1.0
Time Delay (ps)
c
FFT Amplitude
νTO
2νTO
3νTO
4νTO
1
0.1
0.01
0
20
40
60
80
Frequency (THz)
Amplitude QIR (Å√amu)
-2
-1
0
1
2
d
e
f

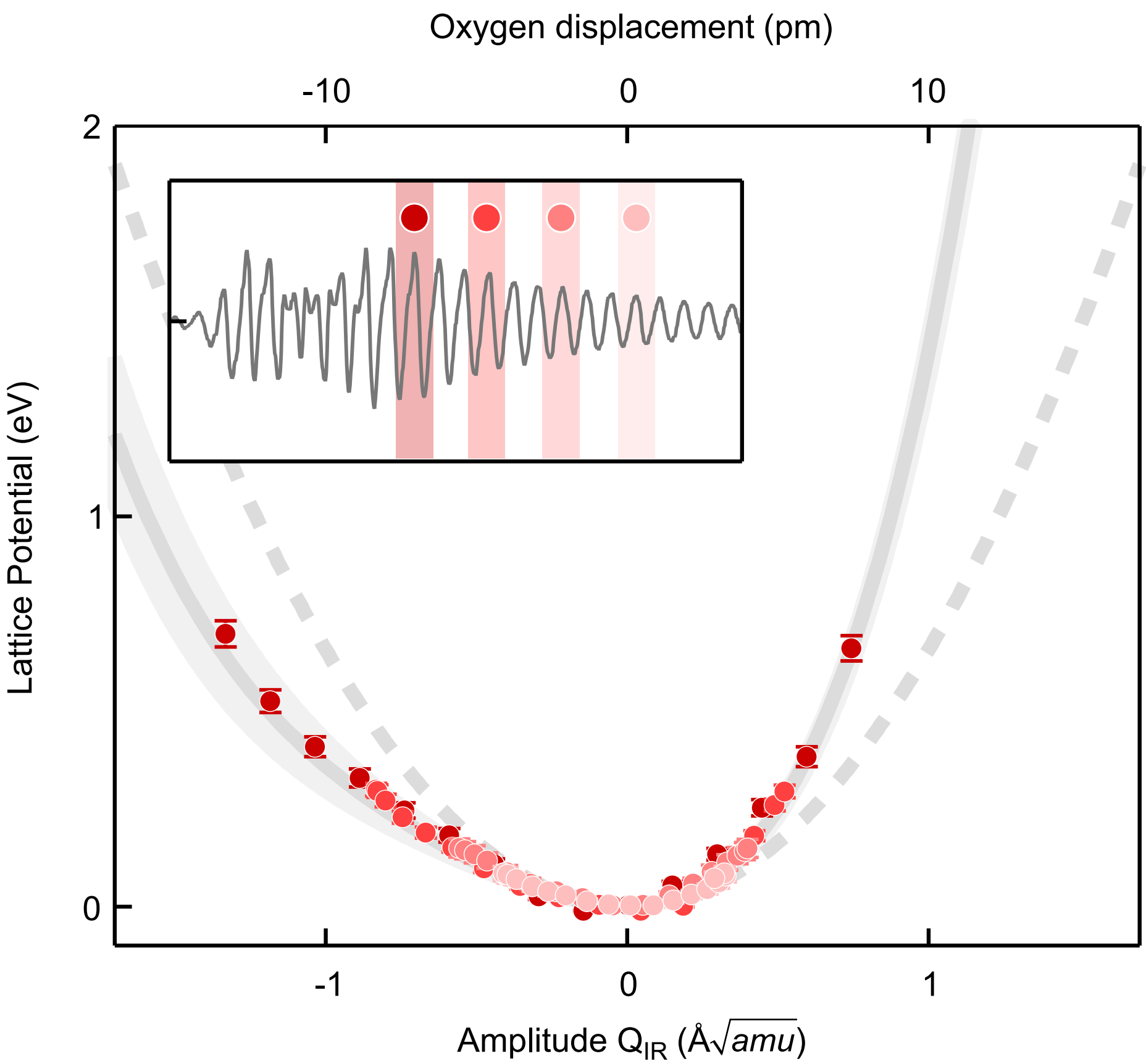
Oxygen displacement (pm)
-10
0
10
2
1
0
Lattice Potential (eV)
-1
0
1
Amplitude Q_{IR} (Å$\sqrt{amu}$)